Tunnel-Field-Effect Spin Filter from Two-Dimensional Antiferromagnetic Stanene

E. G. Marin,[*] D. Marian,[*] G. Iannaccone, and G. Fiori[†]

Dipartimento di Ingegneria dell'Informazione, Università di Pisa, Pisa 56122, Italy

We propose a device concept, based on monolayer stanene, able to provide highly polarized spin currents (up to 98%) with voltage-controlled spin polarization operating at room temperature and with small operating voltage (0.3 V). The concept exploits the presence of spin-polarized edge states in a stanene nanoribbon. The spin polarization of the total current can be modulated by a differential tuning of the transmission properties, and of the occupation of edge states of different spin, via the application of an in-plane electric field. We demonstrate device operation using *ab initio* and quantum-transport simulations.

I. INTRODUCTION

Spintronics, the application of the electron-spin degree of freedom to information technology [1–3], has experimented an impressive progress since the discovery of the giant magneto-resistive effect in the late 1980s [4], which was followed and improved, a few years later, by the tunneling magnetoresistance effect [5]. Nowadays, spintronics constitutes an intense research area embracing many disciplines from physics to computer science [6,7], and involving exciting and promising fields, such as topological insulators [8] and quantum computing [9].

Although many issues are still at their infancy, including efficient injection, transport, and control of spin currents [10,11], enormous progresses have been made, and some notable devices have been proposed and demonstrated, such as, e.g., spin-torque memories, [12–14] spin valves in hard-drive read heads [15], galvanic isolators [16], magnetic memories based on tunnel junctions [17], spin transistors [18], and logic devices built from diluted magnetic semiconductors [19].

Further progresses are expected to be enabled by the investigation of promising combinations of materials and structures [20,21], including ferromagnetics stacks [22], half metals [23,24], or spin-gapless semiconductors [25, 26]. More recently, the rise of graphene [27] opened new possibilities in the field [28,29], unveiling new two-dimensional (2D) materials as potential candidates to be used in spin devices [30–34]. Specifically for graphene, half metallicity in zig-zag nanoribbons [24,35], defect-induced magnetism [36,37], and spin transport at room temperature [38,39] have been predicted and experimentally demonstrated.

In addition to graphene, other column-IV 2D materials [40], like silicene [41], germanene [42], and lastly stanene [43] have been recently pointed out to have a stable antiferromagnetic (AFM) ground state when cut in thin zig-zag nanoribbons [44,45]. A very promising property for spintronics in graphene, germanene, and silicene is the electric-field-controlled half metallicity, i.e., the possibility to tune the nanoribbon band gap from semiconducting to zero with a transversal in-plane electric field, which unfortunately is too large (from 10 to 25 MV/cm) to be used in realistic applications and with practical dielectrics [24,46].

In this letter, we explore the appearance of half metallicity in stanene nanoribbons with first-principles calculations, and we propose a device based on interband tunneling able to exploit this effect to generate highly spin-polarized currents with small and realistic electric fields. We opt for stanene amongst group-IV candidates because it provides a reasonable compromise between the band-gap width (required to avoid high leakage currents) and the transversal electric field necessary to achieve half metallicity (that must prevent the dielectric breakdown). In particular, the high sensitivity of interband tunneling to small modulations of the band gap and its reduced dependence on temperature, together with its robustness against the presence of defects [52], allows us to take advantage of the electric-field-controlled half metallicity in a tunnel FET (TFET) based on a stanene nanoribbon.

A schematic illustration of device operation is shown in Fig. 1. In a TFET, the source and drain regions are *p* and *n* doped, respectively, pinning the chemical potential at the source close to the valence band and the chemical potential at the drain close to the conduction band. At equilibrium, i.e, when no external voltages are applied, the chemical potential along the device is constant. When a positive drain-to-source voltage is considered, the chemical potential at the drain is lowered with respect to the

---

[*]These authors contributed equally to this work.
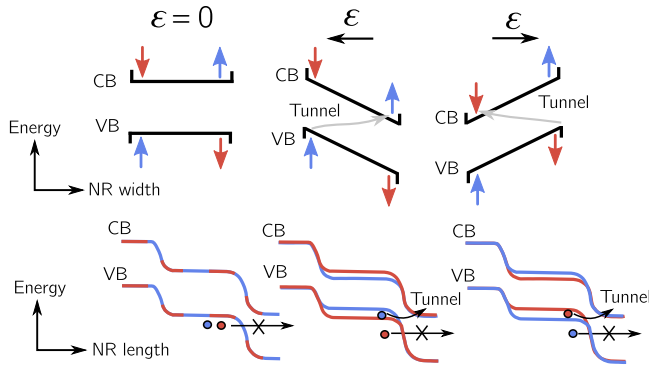
[†]g.fiori@iet.unipi.it

FIG. 1.   Schematic of the device operation principle. Schematic of the stanene nanoribbon (NR), conduction band (CB), and valence band (VB) along the nanoribbon width (top panel) and length (bottom panel) for spin-up (blue) and spin-down (red) carriers, without and with an applied transversal electric field.

source and an energy window for carrier tunneling is open. Then, when no transversal electric field is applied (left) the band gap at any point along the channel is the same for both kinds of spins. If the source and drain regions are properly doped, the window for electron tunneling will face a thick barrier and the current will be small. An in-plane electric field applied in the transversal direction alters the band gap for spin-up and spin-down carriers in the channel. As a consequence, the tunneling probability, from the valence-band states in one edge to the conduction-band states of the opposite edge, increases. The band-gap modulation and, therefore, the selective spin tunneling are due to the AFM configuration, which is predicted to be preserved only for very thin nanoribbons (approximately 1 nm). The implementation of the band-gap modulation in a TFET permits large spin-controlled currents to be obtained with small modulations of the band gap, or equivalently small electric fields, by properly aligning the undoped channel with the doped drain-end region (bottom panel).

II. METHODS

In order to demonstrate the operation of the proposed device concept we adopt a multiscale simulation approach, with *ab initio* calculations of the stanene band structure combined with self-consistent simulations of quantum transport and electrostatics.

Density-functional theory (DFT) as implemented in the Quantum Espresso suite [49], is used to determine the electronic band structure of a zig-zag stanene nanoribbon passivated at the edges with H atoms (Fig. 2). For the DFT calculations, a vacuum of 32 Å and 20 Å in the direction of the nanoribbon width and the direction orthogonal to the nanoribbon plane, respectively,

are assumed to minimize the interaction between periodic repetitions of the cell. We perform a structural optimization within the Broyden-Fletcher-Goldfarb-Shanno algorithm until forces are smaller than 5×10^{-3} eV/Å with a convergence threshold for energy of 10^{-6} eV. A Perdew-Burke-Ernzerhof exchange-correlation functional is used [50] within fully relativistic norm-conserving pseudopotentials. Spin-polarized calculation, within the local spin-density approximation (LSDA) and magnetization along the $\hat{z}$ axis is considered. The pseudopotentials are obtained from the SSSP Library, for both Sn and H [51]. Energy cuttoffs for charge density and wavefunction expansions are set to 360 and 30 Ry, respectively. Integration in the Brillouin zone is accomplished in a $1 \times 10 \times 1$ Γ-centered grid.

The device simulations are based on the self-consistent solution of the three-dimensional Poisson equation, together with the open-boundary Schrödinger equation, within the nonequilibrium Green function (NEGF) [53] formalism, formulated within a tight-binding (TB) scheme [54,55]. For this purpose, we project the plane-wave DFT basis set into a maximally localized Wannier function (MLWF) basis set, exploiting Wannier90 code [56], resulting in Hamiltonians of 96 nearest neighbors for both spin-up and spin-down states. Details of the adopted multiscale approach can be found in [54,57].

III. RESULTS

We consider the stanene zig-zag nanoribbon shown in Fig. 2.

As for graphene, stanene is characterized by a honeycomb lattice (with a unit vector of 4.7 Å), but with a buckled structure with two parallel planes of atoms separated by 0.82 Å [43]. The considered nanoribbon width is 1.29 nm: for such a thin nanoribbon, a large exchange interaction between the edges is expected, preserving magnetism at room temperature [47,48]. While spin-orbit coupling (SOC) is crucial for the appearance of topological spin-polarized edge states in topological insulators, in the antiferromagnetic configuration the spin polarization emerges due to the interedge exchange and SOC plays a minor role. In particular, for the studied system we observe that the calculations including SOC have a negligible impact on the band structure and the sensibility to the electric field is not modified.

In the absence of electric field, the stanene band structure for spin up and down is degenerate [Figs. 2(b) and 2(c), black circles], with an energy band gap of approximately 0.25 eV. The states close to the conduction-band minimum (CBM) and the valence-band maximum (VBM) are localized at the edges of the nanoribbon, and according to the antiferromagnetic configuration, present opposite spin [45,52]. By applying a positive transversal electric field, $\mathbf{E} = E_x \hat{x}$ [Fig. 2(a)], the energy band gap increases
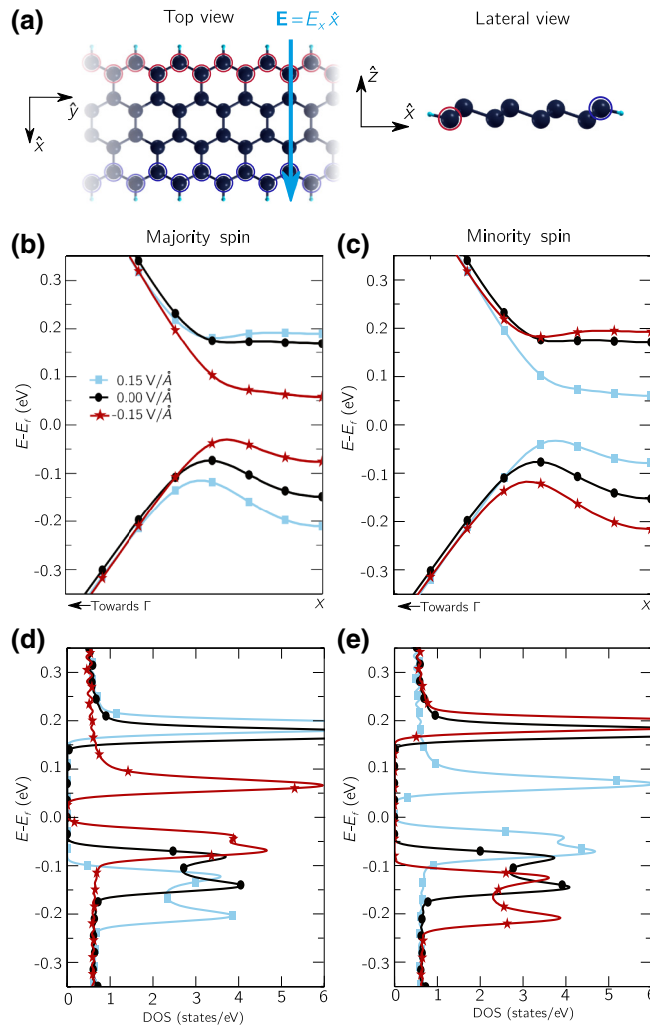
FIG. 2. Crystal and band structure of the stanene nanoribbon. (a) Top and lateral view of the stanene zig-zag nanoribbon (1.26-nm wide) passivated with H atoms. The electric field, $\mathbf{E} = E_x \hat{x}$ is applied along the nanoribbon width. (b),(c) Electronic band structure and (d),(e) density of states for spin-up (left) and spin-down (right) states for several electric fields.

FIG. 3. Schematic of the proposed device. The stanene zig-zag NR is embedded in top, bottom, and lateral SiO$_2$, with thicknesses $t_{ox} = 1$ nm and $t_{lat} = 1$ nm. Two lateral metallic contacts control the spin-current flow. Inset: top view of the device. $L_{ch} = 16.9$ nm, $L_{s/d} = 5.6$ nm, and a doping molar fraction 1.2×10^{-2} are considered for the p- and n-type source and drain.

for spin-up bands and decreases for spin-down bands: the opposite behavior occurs for negative $\mathbf{E}$. For example, for $E_x = 0.15$ V/Å, the spin-down band gap reduces to 0.087 eV, and for spin-up increases to 0.296 eV [Figs. 2(b) and 2(c)].

As can be seen in Figs. 2(d) and 2(e), the small curvature of the stanene band structure around the CBM and the VBM leads to corresponding peaks in the DOS. Coherently with Figs. 2(b) and 2(c) the spin-up and spin-down DOS have opposite dependence on E_x. Eventually, for $E_x = \pm 0.3$ V/Å, the material becomes a half metal (zero band gap). A similar magnitude of the electric field is necessary to achieve half metallicity in graphene, silicene, and germanene [24,46]. These values are, however, larger than the breakdown fields of practical dielectrics, and a device
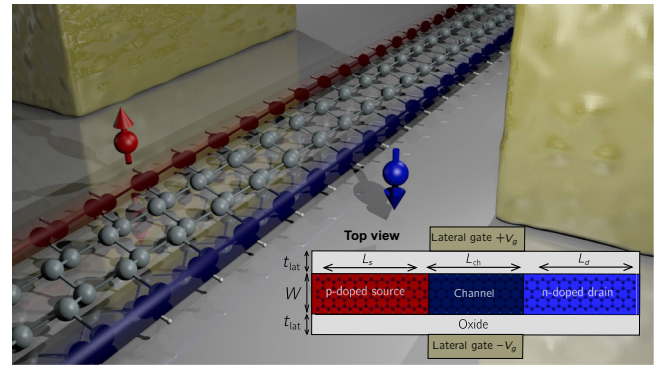
design sensitive to a small modulation of the band gap is mandatory to take practical advantage of this effect in spintronics.

For this purpose, we propose a TFET structure where the stanene nanoribbon is embedded in SiO$_2$, and sandwiched between two lateral metallic contacts, placed 1 nm away from each nanoribbon edge (Fig. 3). The current flow is enabled by interband tunneling between the undoped-channel valence band (VB) and the doped-drain conduction band (CB), but—differently from a TFET—the switching current modulation is due to the modulation of the channel band gap. The interband tunneling current is extremely sensitive to band-gap variations, so that with small electric fields it is possible to tune the alignment between the VB and the CB and consequently achieve large modulation of the spin-polarized current.

The considered nanoribbon has a length of 28.2 nm. At the nanoribbon's ends, we assume 5.64-nm-long p- and n-doped regions, with acceptor and donor molar fractions equal to 1.2×10^{-2}. The 16.9-nm-long central region is the device channel. The two lateral gates are used to create a transversal electric field that, depending on its sign, allows the channel band gap for each spin component to be opened and closed.

In order to accurately study the performance of the proposed device, we perform transport simulations solving self-consistently the three-dimensional Poisson equation, together with the open-boundary Schrödinger equation (see Methods). Spin-up and spin-down polarized currents ($I_{ds}^{\uparrow/\downarrow}$) in the ballistic regime at room temperature ($T = 300$ K) are calculated exploiting Landauer's formalism [58,59].

In order to illustrate the working principle of the proposed device, we depict the DOS as a function of energy (refered to the Fermi level at the source lead), and the
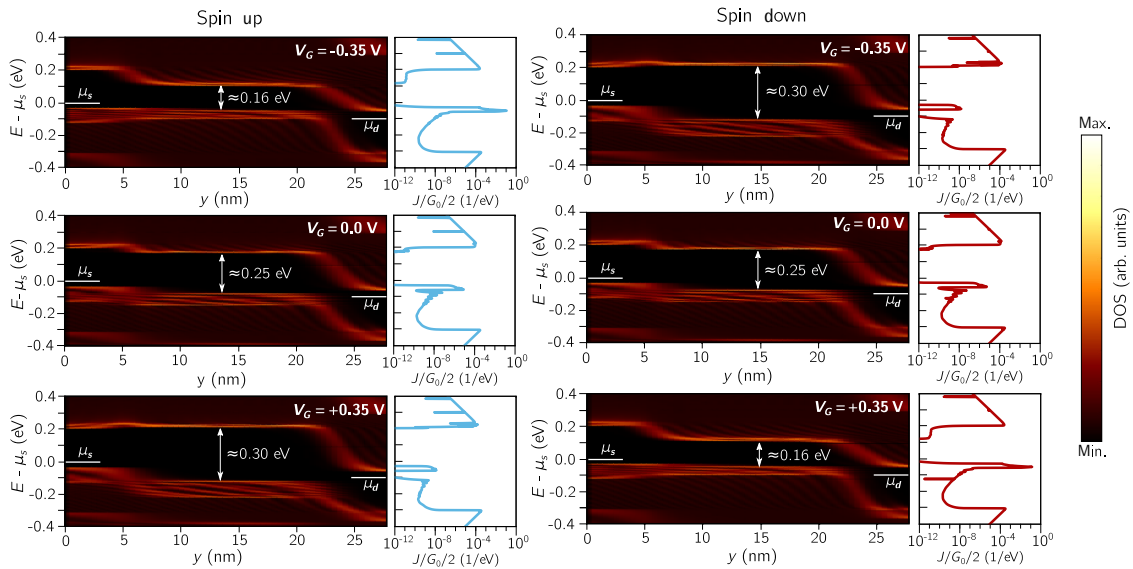
FIG. 4. DOS and current-density spectrum. DOS as a function of energy and longitudinal position along the nanoribbon for the spin-up (left) and spin-down (right) carriers for several applied voltages (V_G), for a drain-to-source voltage of $V_{ds} = 0.1$ V. Next to each DOS colormap is the current-density spectrum in semilogarithmic scale normalized to half the conductance quantum.

position along the nanoribbon length (y), for both spin-up and spin-down carriers (Fig. 4). On the right-hand side of each DOS plot, we include the spectrum of the current density for the corresponding spin, normalized to half the conductance quantum ($G_0/2 = q^2/h$) in semilogarithmic scale. A drain-to-source voltage $V_{ds} = 0.1$ V and several values of V_G are considered. The Fermi level at the source (μ_s) and drain (μ_d) leads are depicted together with the gap value at the channel. From the DOS colormap, one can easily recognize the CB and VB, which correspond to two high-DOS stripes. The energy gap is also identified as a zero-DOS region between the CB and VB. As can be seen, in the channel region (5.6 nm < y < 22.5 nm) the band-gap width is modulated by V_G, while it remains invariant at the source and drain regions where the influence of the gates is negligible. The device behavior is thus explained as follows: when $V_G = 0$ V (Fig. 4 center panel) spin-down and spin-up carriers face equal barriers for interband tunneling and the current-density spectrum (normalized to $G_0/2$) does not show significant differences, and therefore the total current has no spin polarization. In contrast, when $V_G \neq 0$ V spin-up and spin-down carriers experience different channel interband-tunneling band gap and consequently the current has spin polarization.

In particular, for $V_G = -0.35$ V (Fig. 4 top panel), the band gap for the spin-down states widens (approximately 0.30 eV) whilst it closes (approximately 0.16 eV) for spin-up states. As a consequence, when the channel band gap is increased the interband (from the channel VB to the drain CB) tunneling probability is reduced, resulting in a decrease of the spin-down current, until only the thermionic components are visible. On the other hand, as

the channel band gap is reduced for spin-up states, the carriers from the p-doped source VB fill the channel VB, and tunnel through the channel-VB-to-drain-CB thin barrier, notably increasing the tunneling current for this spin component, as shown by the current-density spectrum, and resulting in a highly spin-polarized total current. Symmetrically opposite behavior is observed for $V_G = 0.35$ V (Fig. 4 bottom panel).

The spin-to-total current ratio as well as the total current and the spin-up and spin-down components are shown as a function of the applied gate voltage in Fig. 5, for $V_{ds} = 0.1$ V. The total current (gray squares) shows a symmetric behavior with a minimum at $V_G = 0$ V, when current has no spin polarization, as spin-up (red circles) and spin-down (blue triangles) currents provide equal contribution. If a
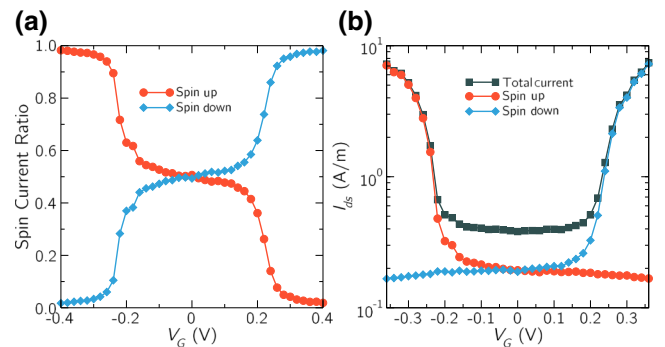

FIG. 5. Spin currents. (a) Spin-to-total current ratio and (b) Total current and spin components in semilogarithmic scale, as a function of the voltage applied at the lateral gates (V_G), for a drain-to-source voltage of $V_{ds} = 0.1$ V.

nonzero V_G is applied, the symmetry is broken, and the total current becomes slightly spin polarized with spin-up for $V_G > 0$ and spin-down for $V_G < 0$. The spin polarization of the current increases with V_G and achieves 90% for $V_G = \pm0.2$ V, and 98% for $V_G = \pm0.3$ V.

IV. DISCUSSION

We theoretically demonstrate the electrical behavior of a device based on 2D stanene, able to provide tunable spin-polarized current up to a polarization of 98% with a small applied voltage on the controlling electrode. The proposed device is based on the modulation of the band gap of narrow stanene nanoribbons and the edge-localized nature of the conduction- and valence-band states. Taking advantage of this property, the device controls the interband tunneling currents through electric-field modulation of the energy band gap, achieving a spin polarization as high as 98% with electric field of 0.3 V/nm. We think that the proposed device might be useful to explore new concepts of spin injectors or filters, which are the fundamental building blocks of spintronics.

ACKNOWLEDGMENTS

[1] S. A. Wolf, D. D. Awschalom, R. A. Buhrman, J. M. Daughton, S. Von Molnar, M. L. Roukes, A. Y. Chtchelkanova, and D. M. Treger, Spintronics: A spin-based electronics vision for the future, Science **294**, 1488 (2001).

[2] D. D. Awschalom and M. E. Flatté, Challenges for semiconductor spintronics, Nat. Phys. **3**, 15 (2007).

[3] C. Felser, G. H. Fecher, and B. Balke, Spintronics: A challenge for materials science and solid-state chemistry, Ang. Chem. Int. Ed. **46**, 668 (2007).

[4] M. N. Baibich, J. M. Broto, A. Fert, F. N. Van Dau, F. Petroff, P. Etienne, G. Creuzet, A. Friederich, and J. Chazelas, Giant Magnetoresistance of (001) Fe/(001) Cr Magnetic Superlattices, Phys. Rev. Lett. **61**, 2472 (1988).

[5] J. S. Moodera, L. R. Kinder, T. M. Wong, and R. Meservey, Large Magnetoresistance at Room Temperature Inferromagnetic Thinfilm Tunnel Junctions, Phys. Rev. Lett. **74**, 3273 (1995).

[6] Y. Xu, D. D. Awschalom, and J. Nitta, *Handbook of Spintronics* (Springer Publishing, Amsterdam, 2016).

[7] I. Zutic, J. Fabian, and S. Das Darma, Spintronics: Fundamentals and applications, Rev. Mod. Phys. **76**, 323 (2004).

[8] X. L. Qi and S. C. Zhang, Topological insulators and superconductors, Rev. Mod. Phys. **83**, 1057 (2011).

[9] M. N. Leuenberger and D. Loss, Quantum computing in molecular magnets, Nature **410**, 789 (2001).

[10] C. O. Avci, A. Quindeau, C. F. Pai, M. Mann, L. Caretta, A. S. Tang, M. C. Onbasli, C. A. Ross, and G. S. Beach, Current-induced switching in a magnetic insulator, Nat. Mat. **16**, 309 (2017).

[11] I. M. Miron, K. Garello, G. Gaudin, P. J. Zermatten, M. V. Costache, S. Auffret, S. Bandiera, B. Rodmacq, A. Schuhl, and P. Gambardella, Perpendicular switching of a single ferromagnetic layer induced by in-plane current injection, Nature **476**, 189 (2011).

[12] L. Liu, C. F. Pai, Y. Li, H. W. Tseng, D. C. Ralph, and R. A. Buhrman, Spin-torque switching with the giant spin Hall effect of tantalum, Science **336**, 555 (2012).

[13] M. Hosomi, H. Yamagishi, T. Yamamoto, K. Bessho, Y. Higo, K. Yamane, H. Yamada, M. Shoji, H. Hachino, C. Fukumoto, and H. Nagao, A novel nonvolatile memory with spin torque transfer magnetization switching: Spin-RAM, IEDM Tech. Digest. IEEE Int. 459 (2005).

[14] G. Prenat, K. Jabeur, G. D. Pendina, O. Boulle, and G. Gaudin, *Spin Orbit Torque RAM SOT-MRAM for High Speed and High Reliability Applications* (Springer Publishing, Zurich, 2015), Vol. 145.

[15] C. Tsang, R. E. Fontana, T. Lin, D. E. Heim, V. S. Speriosu, B. A. Gurney, and M. L. Williams, Design, fabrication and testing of spin-valve read heads for high density recording, IEEE Trans. Magn. **30**, 3801 (1994).

[16] T. M. Hermann, W. C. Black, and S. Hui, Magnetically coupled linear isolator, IEEE Trans. Magn. **33**, 4029 (1997).

[17] W. J. Gallagher and S. S. Parkin, Development of the magnetic tunnel junction MRAM at IBM: From first junctions to a 16-Mb MRAM demonstrator chip, IBM J. Res. Dev. **50**, 5 (2006).

[18] S. Datta and S. Das Darma, Electronic analog of the electrooptic modulator, App. Phys. Lett. **56**, 665 (1990).

[19] H. Ohno, D. Chiba, F. Matsukura, T. Omiya, E. Abe, T. Dietl, Y. Ohno, and K. Ohtan, Electric-field control of ferromagnetism, Nature **408**, 944 (2000).

[20] H. Ohono, M. D. Styles, and B. Dieny, Spintronics, Proc. IEEE **104**, 1782 (2016).

[21] G. Y. Gao and K. L. Yao, Antiferromagnetic half-metals, gapless half-metals, and spin gapless semiconductors: The D03-type Heusler alloys,, App. Phys. Lett. **103**, 232409 (2013).

[22] F. J. Jedema, A. T. Filip, and B. J. Van Wees, Electrical spin injection and accumulation at room temperature in an all-metal mesoscopic spin valve, Nature **410**, 345 (2001).

[23] R. A. De Groot, F. M. Mueller, P. G. Van Engen, and K. H. J. Buschow, New Class of Materials: Half-Metallic Ferromagnets, Phys. Rev. Lett. **50**, 2024 (1983).

[24] Y-W. Son, M. L. Cohen, and S. G. Louie, Half-metallic graphene nanoribbons, Nature **446**, 342 (2006).

[25] X. L. Wang, Proposal for a New Class of Materials: Spin Gapless Semiconductors, Phys. Rev. Lett. **100**, 156404 (2008).

[26] S. Ouardi, G. H. Fecher, C. Felser, and J. Kübler, Realization of Spin Gapless Semiconductors: The Heusler Compound Mn2CoAl, Phys. Rev. Lett. **110**, 100401 (2013).

[27] K. S. Novoselov, A. K. Geim, S. V. Morozov, D. Jiang, Y. Zhang, S. V. Dubonos, I. V. Grigorieva, and A. A. Firsov, Electric field effect in atomically thin carbon films, Science **306**, 666 (2004).

[28] S. Roche, J. Akerman, B. Beschoten, J. C. Charlier, M. Chshiev, S. P. Dash, B. Dlubak, J. Fabian, A. Fert, M Guimaraes, and F. Guinea, Graphene spintronics: The European Flagship perspective, 2D Mater. **2**, 030202 (2015).

[29] W. Han, R. K. Kawakami, M. Gmitra, and J. Fabian, Graphene spintronics, Nat. Nano **9**, 794 (2014).

[30] J. H. Garcia, M. Vila, A. W. Cummings, and S. Roche, Spin transport in graphene/transition metal dichalcogenide heterostructures, Chem. Soc. Rev. **47**, 3359 (2018).

[31] D. Pesin and A. H. Macdonald, Spintronics and pseudospintronics in graphene and topological insulators, Nat. Mat. **11**, 409 (2012).

[32] G. Gao, G. Ding, J. Li, K. Yao, M. Wu, and M. Qian, Monolayer MXenes: Promising half-metals and spin gapless semiconductors, Nanoscale **8**, 8986 (2016).

[33] Y. Nie, M. Rahman, P. Liu, A. Sidike, Q. Xia, and G. H. Guo, Room-temperature half-metallicity in monolayer honeycomb structures of group-V binary compounds with carrier doping, Phys. Rev. B **96**, 075401 (2017).

[34] M. Ashton, D. Gluhovic, S. B. Sinnott, J. Guo, D. A. Stewart, and R. G. Hennig, Two-dimensional intrinsic half-metals with large spin haps, Nano Lett. **17**, 5251 (2017).

[35] E. J. Kan, Z. Li, J. Yang, and J. G. Hou, Half-metallicity in edge-modified zigzag graphene nanoribbons, J. Ame. Chem. Soc. **130**, 4224 (2008).

[36] O. V. Yazyev and L. Helm, Defect-induced magnetism in graphene, Phys. Rev. B **75**, 125408 (2007).

[37] J. Bundesman, M-H. Liu, I. Adagideli, and K. Richter, Spin conductance of diffusive graphene nanoribbons: A probe of zig-zag edge magnetization, Phys. Rev. B **88**, 195406 (2013).

[38] N. Tombros, C. Jozsa, M. Popinciuc, H. T. Jonkman, and B. J. Van Wees, Electronic spin transport and spin precession in single graphene layers at room temperature, Nature **448**, 571 (2007).

[39] W. Han, K. Pi, K. M. McCreary, Y. Li, J. J. Wong, A. G. Swartz, and R. K. Kawakami, Tunneling Spin Injection into Single Layer Graphene, Phys. Rev. Lett. **105**, 167202 (2010).

[40] A. Molle, J. Goldberger, M. Houssa, Y. Xu, S. C. Zhang, and D. Akinwande, Buckled two-dimensional Xene sheets, Nat. Mat. **16**, 163 (2017).

[41] P. Vogt, P. de Padova, C. Quaresima, J. Avila, E. Frantzeskakis, M.-C. Asensio, A. Resta, B. Ealet, and G. Le Lay, Silicene: Compelling Experimental Evidence for Graphene-Like Two-Dimensional Silicon, Phys. Rev. Lett. **108**, 155501 (2012).

[42] M. E. Davila, L. Xian, S. Cahangirov, A. Rubio, and G. Le Lay, Germanene: A novel two-dimensional germanium allotrope akin to graphene and silicene, New J. Phys. **16**, 095002 (2014).

[43] F. F Zhu, W. J. Chen, Y. Xu, C. L. Gao, D. D. Guan, C. H. Liu, D. Qian, S. C. Zhang, and J. F. Jia, Epitaxial growth of two-dimensional stanene, Nat. Mat. **14**, 1020 (2015).

[44] T-C. Wang, C-H. Hsu, Z-Q. Huang, F-C. Chuang, W-S. Su, and G-Y. Guo, Tunable magnetic states on the zig-zag edges if hydrogenated and halogenated group-IV nanoribbons, Sci. Rep. **6**, 39083 (2016).

[45] W. Xiong, C. Xia, Y. Peng, J. Du, T. Wang, J. Zhang, and Y. Jian, Spin-orbit coupling effects on electronic structures in stanene nanoribbons, Phys. Chem. Chem. Phys. **18**, 6534 (2016).

[46] Y. Wang, J. Zheng, Z. Ni, R. Fei, Q. Liu, R. Quhe, C. Xu, J. Zhou, Z. Gao, and J. Lu, Half-metallic silicene and germanene nanoribbons: Towards high-performance spintronics device, Nano **7**, 1250037 (2012).

[47] J. Jung, T. Pereg-Barnea, and A. H. MacDonald, Theory of Interedge Superexchange in Zig-Zag Edge Magnetism, Phys. Rev. Lett. **102**, 227205 (2009).

[48] O. V. Yazyev, Emergence of magnetism in graphene materials and nanostructures, Rep. Prog. Phys. **73**, 056501 (2010).

[49] P. Giannozzi, S. Baroni, N. Bonini, M. Calandra, R. Car, C. Cavazzoni, D. Ceresoli, G. L. Chiarotti, M. Cococcioni, I. Dabo, A. Dal Corso, S. de Gironcoli, S. Fabris, G. Fratesi, R. Gebauer, U. Gerstmann, C. Gougoussis, A. Kokalj, M. Lazzeri, L. Martin-Samos, N. Marzari, F. Mauri, R. Mazzarello, S. Paolini, A. Pasquarello, L. Paulatto, C. Sbraccia, S. Scandolo, G. Sclauzero, A. P. Seitsonen, A. Smogunov, P. Umari, and R. M. Wentzcovitch, QUANTUM ESPRESSO: A modular and open-source software project for quantum simulation of materials, J. Phys.: Cond. Matt. **21**, 395502 (2009).

[50] J. P. Perdew, K. Burke, and M. Ernzerhof, Generalized Gradient Approximation Made Simple, Phys. Rev. Lett. **77**, 3865 (1996).

[51] Standard Solid State Pseudopotentials (SSSP), http://www.materialscloud.org/sssp, (2017).

[52] E. G. Marin, D. Marian, G. Iannaccone, and G. Fiori, First principle investigation of Tunnel FET based on nanoribbons from topological two-dimensional material, Nanoscale **9**, 19390 (2017).

[53] S. Datta, Nanoscale device modeling: The Greens function method, Superlatt. Microstruc. **28**, 253 (2000).

[54] E. G. Marin, M. Perucchini, D. Marian, G. Iannaccone, and G. Fiori, Modeling of electron devices based on two-dimensional materials, IEEE Trans. Elec. Dev. **85**, 4167 (2018).

[55] Nano TCAD ViDES. 2017, available at: http://vides.nanotcad.com/vides/.

[56] N. Marzari, A. A. Mostofi, J. R. Yates, I. Souza, and D. Vanderbilt, Maximally localized Wannier functions: Theory and applications, Rev. Mod. Phys. **84**, 1419 (2012).

[57] G. Pizzi, M. Gibertini, E. Dib, N. Marzari, G. Iannaccone, and G. Fiori, Performance of arsenene and antimonene double-gate MOSFETs from first principles, Nat. Comm. **7**, 1 (2016).

[58] R. Landauer, Spatial variation of currents and fields due to localized scatterers in metallic conduction, IBM J. Res. Dev. **32**, 306 (1988).

[59] M. Buttiker, Scattering Theory of Thermal and Excess Noise in Open Conductors, Phys. Rev. Lett. **65**, 2901 (1990).